



HAL
open science

The Role of Superadsorbent Polymers on Covalent Organic Frameworks-Based Solid Electrolytes: Investigation of the Ionic Conductivity and Relaxation

Sara Gullace, Luca Cusin, Fanny Richard, Nizami Israfilov, Artur Ciesielski,
Paolo Samorì

► **To cite this version:**

Sara Gullace, Luca Cusin, Fanny Richard, Nizami Israfilov, Artur Ciesielski, et al.. The Role of Superadsorbent Polymers on Covalent Organic Frameworks-Based Solid Electrolytes: Investigation of the Ionic Conductivity and Relaxation. *Advanced Materials Interfaces*, 2023, 10.1002/admi.202300124 . hal-04100628

HAL Id: hal-04100628

<https://hal.science/hal-04100628>

Submitted on 17 May 2023

HAL is a multi-disciplinary open access archive for the deposit and dissemination of scientific research documents, whether they are published or not. The documents may come from teaching and research institutions in France or abroad, or from public or private research centers.

L'archive ouverte pluridisciplinaire **HAL**, est destinée au dépôt et à la diffusion de documents scientifiques de niveau recherche, publiés ou non, émanant des établissements d'enseignement et de recherche français ou étrangers, des laboratoires publics ou privés.

The Role of Superadsorbent Polymers on Covalent Organic Frameworks-Based Solid Electrolytes: Investigation of the Ionic Conductivity and Relaxation

Sara Gullace, Luca Cusin, Fanny Richard, Nizami Israfilov, Artur Ciesielski,*
and Paolo Samorì*

The scarcity of fossil fuels calls for immediate action toward the development of clean and renewable energy resources. In this context, proton exchange membrane fuel cells (PEMFCs) are gaining ever-increasing attention as clean technology. Although covalent organic frameworks (COFs) do not usually exhibit high intrinsic proton conductivity (σ), they have been recently proposed as solid polymer electrolytes in PEMFCs, thanks to their high crystallinity and stability to acids and bases. Here, a simple strategy is presented to improve the performance of poor COF-based proton conductors through addition of sodium polyacrylate (PANA) superadsorbent polymer. Electrochemical impedance spectroscopy investigations after activation at high temperature and relative humidity (RH) provide insights into the role of PANA, whose presence is key to preserve high σ at low RH. The humidity-dependent X-ray diffraction study reveals a strengthening of the stacking interaction along the COF (100) plane direction with increasing humidity, through the formation of H-bonding, thus promoting proton hopping. The study of the dielectric properties as a function of PANA content enables to determine a Debye relaxation regime for the COF/PANA blend with a maximum relaxation frequency of 1513 and 6606 Hz for the pristine COF and the COF/PANA blend, respectively, at their maximum operating temperatures.

1. Introduction

Fuel cells (FCs) represent a viable alternative to non-renewable energy resources, thanks to their high energy conversion efficiency, low to zero-carbon emission, high durability, and mild operating conditions.^[1] FCs are typically classified by the nature of the employed electrolyte. Recently proton exchange membrane FCs (PEMFCs) received considerable attention, being a clean technology employing hydrogen as fuel and yielding only water and heat as byproducts of the electrochemical reaction. Proton conductors play a significant role in PEMFCs, where they are employed as solid polymer electrolytes (SPEs) in the membrane electrode assembly (MEA)^[2] with cathode and anode. Electric power is generated from the electrochemical redox reactions whenever hydrogen and air are supplied at the electrodes. The proton exchange membrane, or SPE, is typically a polymer that is impermeable to gases and electrons but possesses an excellent proton conductivity (σ).^[1,2] Although several materials have

been already proposed as SPEs, spanning from Nafion and perfluorinated sulfonated polymers to oxo-acids, perovskite-type ceramic oxides and metal-organic frameworks,^[1,3] they usually suffer from high water solubility or low tolerance to acidic guest doping, which limit the operating conditions. Indeed, PEMFCs can be classified on the basis of their operating temperature as low- or high-temperature FCs (LT- or HT-FCs) functioning at 60–80 or 120–180 °C, respectively. While HT-FCs are characterized by improved reaction kinetics at the electrodes, which is accompanied by an accelerated degradation of the components, especially in the MEA, LT-FCs require high humidity to operate, leading to the presence of water molecules existing in liquid and vapor phases.^[4] Indeed, one of the major challenges in the development of PEMFCs consists in water management: hydration of the SPE is fundamental to enhance its σ , but it is detrimental to the cell stability and performance, since condensation, followed by flooding, is inevitable when the operating temperature is ≈ 80 °C.^[5] For all these reasons, recent research effort has been dedicated also to the activation of the FCs

S. Gullace, L. Cusin, F. Richard, A. Ciesielski, P. Samorì
 Université de Strasbourg & CNRS
 Institut de Science et d'Ingénierie Supramoléculaires
 8 Allée Gaspard Monge, Strasbourg 67000, France
 E-mail: ciesielski@unistra.fr; samori@unistra.fr

N. Israfilov
 Université de Strasbourg
 CNRS
 Laboratoire de Tectonique Moléculaire
 4 Rue Blaise Pascal, Strasbourg 67081, France

 The ORCID identification number(s) for the author(s) of this article can be found under <https://doi.org/10.1002/admi.202300124>.

© 2023 The Authors. Advanced Materials Interfaces published by Wiley-VCH GmbH. This is an open access article under the terms of the Creative Commons Attribution License, which permits use, distribution and reproduction in any medium, provided the original work is properly cited.

DOI: 10.1002/admi.202300124

previous to the operation, for example by hydrogen pumping, short circuit, cathode starvation, and boiling or steaming of the MEA.^[6]

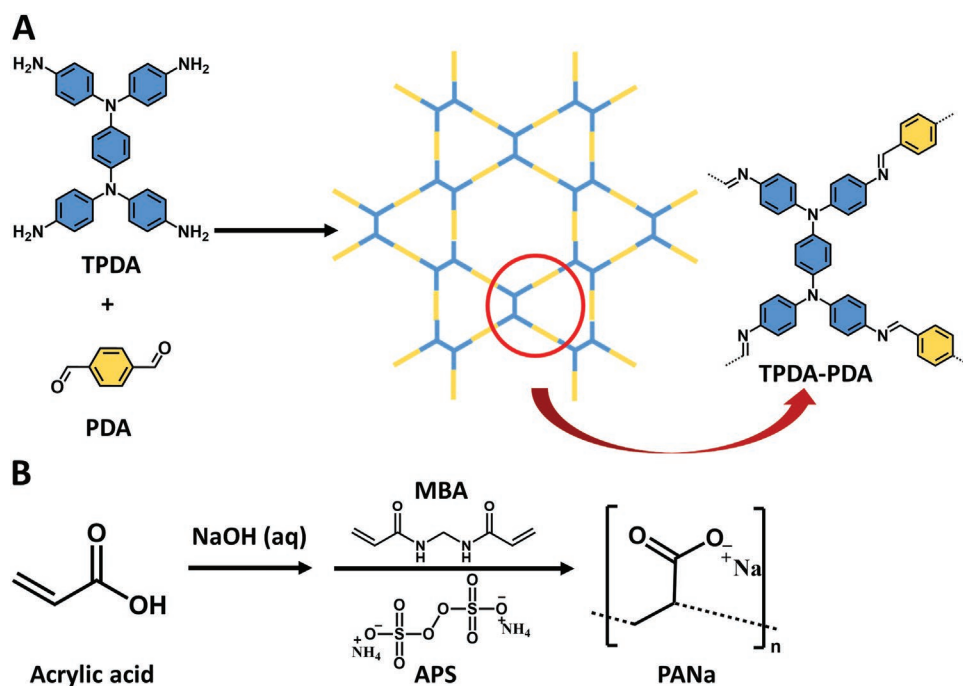
Covalent organic frameworks (COFs) are a class of crystalline porous materials with a high degree of structural complexity and porosity, as well as thermal and chemical stability.^[7] As a consequence of the vast range of topological configurations, COFs are characterized by a highly ordered lattice structure and discrete pores which can interact with photons, electrons, holes, ions, and molecules, giving rise to unique hybrid platforms with diverse functionalities.^[8] The great variability of the properties is directly translated into a wide range of applications, spanning from adsorption of contaminants and molecular sieving to catalysis, sensing, energy storage, and proton conduction.^[1,9,10] Although pristine COFs are not particularly appealing for applications as proton conductors due to the difficult incorporation of proton-donating functionalities in their backbone, they can be combined with several protonic species (phosphoric acid, phytic acid, or N-heterocycles) yielding materials with enhanced proton conducting properties. The first example of such an approach has been reported in 2014 by Chandra et al., who demonstrated that an azo-functionalized COF can achieve σ of $9.9 \times 10^{-4} \text{ S cm}^{-1}$ when loaded with phosphoric acid, while the pristine COF was not intrinsically a proton conductor.^[11] When compared to Nafion, the most commercially used SPE with σ of 10^{-2} – $10^{-1} \text{ S cm}^{-1}$, the main advantages of COFs are the crystallinity, allowing the study of the structure-property relationship, and the high stability to acids or bases, which is fundamental when the pore loading with small acid molecules is proposed to improve σ even at high temperature.^[1,12,13] However, although phosphoric acid doping of the SPE has been widely reported, acid leaching causing oxidative and mechanical degradation of the FC components represents a concerning drawback limiting the applicability of this doping method.^[14] Recently, Shi et al. proposed the use of confined hydrogen-bonded networks, to facilitate the preservation of high σ at low relative humidity (RH). To this end, an ionic COF membrane decorated with $-\text{SO}_3\text{H}$ groups have been employed, aiming at developing weakly humidity-dependent proton exchange membranes, with in-plane σ values $\approx 10^{-1} \text{ S cm}^{-1}$ at 40% RH and 90 °C, after H_2SO_4 soaking at 60 °C for 3 days.^[15] Overall, alternative materials characterized by high crystallinity, high stability to acids or bases and wide operating temperature stability to be used as SPEs are highly sought after.^[16]

In this work, we have investigated the influence of a sodium polyacrylate (PANa) superadsorbent polymer on the proton conduction efficiency of a Kagome-shaped imine-based COF, synthesized through condensation between *N,N,N',N'*-tetrakis(4-aminophenyl)-1,4-benzenediamine (TPDA) and terephthalaldehyde (PDA). Electrochemical impedance spectroscopy (EIS) has been performed by conducting both sample equilibration and measurements at high RH and varying temperatures, or by preliminary equilibration/activation at high RH and temperature followed by measurement at ambient conditions. In this way, we could determine the activation energy for conduction and the best operating temperature for each sample. Overall, we found that when compared to the pristine COF, the addition of PANa in the blend resulted in a σ increase of one order of magnitude, as well as an enhanced maximum operating temperature

(from 60 to 80 °C) and decreased activation energy for the proton conduction. EIS investigations at ambient conditions after equilibration/activation at high temperature and RH provided insights into the role of PANa, whose presence was key to preserve high σ at low RH. For the first time a humidity-dependent X-ray diffraction analysis was performed to support the EIS data, revealing a decrease in the (100) plane lattice distance upon humidification, which may be related to the strengthening of the stacking interaction along this direction via H-bonding, thereby promoting the proton hopping. To the best of our knowledge, dielectric studies on COFs as proton-conducting materials have not been performed yet. An extensive investigation of the relaxation mechanism as a function of PANa content enabled us to determine a Debye relaxation regime for the COF/PANa blends with a maximum relaxation frequency (ω_{max}^M) growing from 1380 to 1585 Hz when the PANa content increased from 100 to 150 μL in the blend. Furthermore, the temperature-dependent dielectric study revealed that the width of frequency range for a long-range motion of charge carriers in the electrolyte increased when comparing the pristine COF and the COF/PANa blend at their maximum operating temperatures, with ω_{max}^M increasing from 1513 to 6606 Hz. Overall, we were able to shed a light onto the effect of a superadsorbent polymer on a poorly proton-conducting COF, correlating the variation of the material's spectroscopic fingerprint with its proton conduction performance and dielectric properties. This study enabled us to demonstrate that the new hybrid material can be efficiently activated to preserve σ at ambient conditions, thereby offering new solutions to the water management problem in PEMFCs.

2. Results and Discussion

A schematic representation of COF TPDA-PDA synthesis from *N,N,N',N'*-tetrakis(4-aminophenyl)-1,4-phenylenediamine (TPDA) and terephthalaldehyde (PDA), as well as COF TPDA-PDA/PANa blend preparation is shown in **Scheme 1**. The solvothermal synthesis of the TPDA-PDA COF yields a powder composed of nanoflower-like crystallites, as shown in Figure S1 (Supporting Information). The synthesis of PANa results in a dense liquid that incubated at 65 °C for 2 h polymerizes forming a highly cross-linked hydrogel displaying a rough and wrinkled surface (Figure S1C, Supporting Information). SEM images in Figure S1 (Supporting Information) and **Figure 1** reveal that TPDA-PDA and TPDA-PDA/150 μL PANa exhibit the same morphology with nanoplatelets featuring the same size, shape, or arrangement. Furthermore, the morphology is also retained when the powders are compressed to form pellets for EIS measurements (Figure S2, Supporting Information). The FT-IR spectrum of TPDA-PDA exhibits the typical bands of an imine-linked COF (Figure 1B), with the presence of the imine C=N stretching at 1644 cm^{-1} , while C=O and C-N bands at 1709 and 1288 cm^{-1} , respectively, appear with significantly reduced intensities compared to the starting monomers, comprising aldehyde and amine moieties (Figure S3A, Supporting Information).^[17,18] The most prominent peak at 1545 cm^{-1} is assigned to the C=C stretching and phenyl rings breathing modes. The FT-IR spectrum of PANa hydrogel in Figure S3B



Scheme 1. Schematic representation of A) the reaction of *N,N,N',N'*-tetrakis(4-aminophenyl)-1,4-phenylenediamine (TPDA) and terephthalaldehyde (PDA) to synthesize COF TPDA-PDA with a Kagome structure, and B) polymerization of acrylic acid in the presence of *N,N'*-Methylenebis(acrylamide) (MBA) and ammonium persulfate (APS) to synthesize PANa.

(Supporting Information) portrays the characteristic bands for the carboxylate symmetric and asymmetric stretching (1428 and 1608 cm^{-1}) and O–H stretching ($3000\text{--}3500\text{ cm}^{-1}$). The presence of PANa in TPDA-PDA/ $150\text{ }\mu\text{L PANa}$ does not influence the IR spectrum when it is acquired after equilibration at $65\text{ }^\circ\text{C}$ and vacuum for 2 h, suggesting the superadsorbent polymer growth does not alter the COF backbone structure. Interestingly, the equilibration of TPDA-PDA/ $150\text{ }\mu\text{L PANa}$ at $80\text{ }^\circ\text{C}$ and 95% RH for 6 h induces the shift of the C=O stretching band to 1696 cm^{-1} and an increase of its intensity: this could be rationalized as a partial hydrolysis of the imine bond through protonation, occurring at high RH in the presence of the superadsorbing polymer. Nonetheless, the imine/aldehyde peak

ratio and position appears to be reversible when the sample is dried again at $65\text{ }^\circ\text{C}$ and vacuum for 1 h (Figure S4, Supporting Information).

TGA has been performed to shed light on the thermal stability of pristine SPE as well as the possible variations caused by addition of PANa. Figure S5A (Supporting Information) shows that TPDA-PDA and TPDA-PDA/ $150\text{ }\mu\text{L PANa}$ are characterized by nearly identical thermogravimetric profiles, with an initial $\approx 17\%$ weight loss in the temperature range between 110 and $170\text{ }^\circ\text{C}$, associated to the loss of water, followed by the decomposition occurring after $500\text{ }^\circ\text{C}$. The differential TGA spectra in Figure S5B (Supporting Information) highlight that the second weight loss takes place at 158 and $170\text{ }^\circ\text{C}$ for the pristine COF

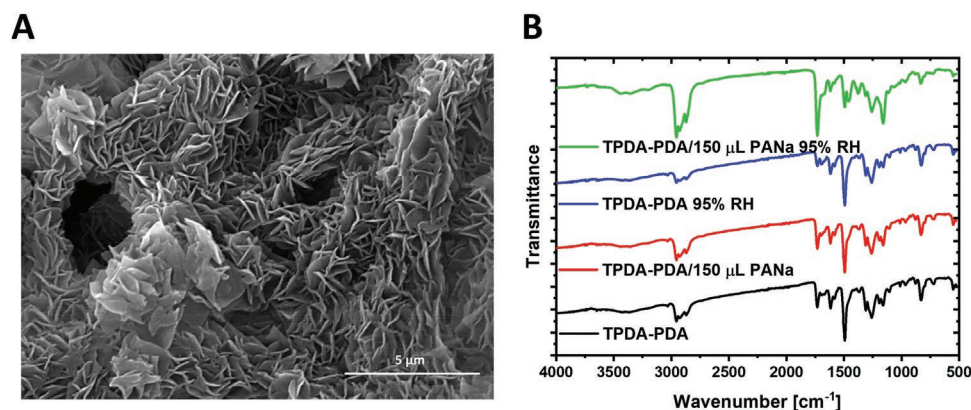


Figure 1. A) Scanning electron microscopy image of TPDA-PDA/ $150\text{ }\mu\text{L PANa}$. B) FT-IR spectra of (black) TPDA-PDA and (red) TPDA-PDA/ $150\text{ }\mu\text{L PANa}$ after equilibration at $65\text{ }^\circ\text{C}$ and vacuum, and (blue) TPDA-PDA and (green) TPDA-PDA/ $150\text{ }\mu\text{L PANa}$ after equilibration at $80\text{ }^\circ\text{C}$ and 95% RH.

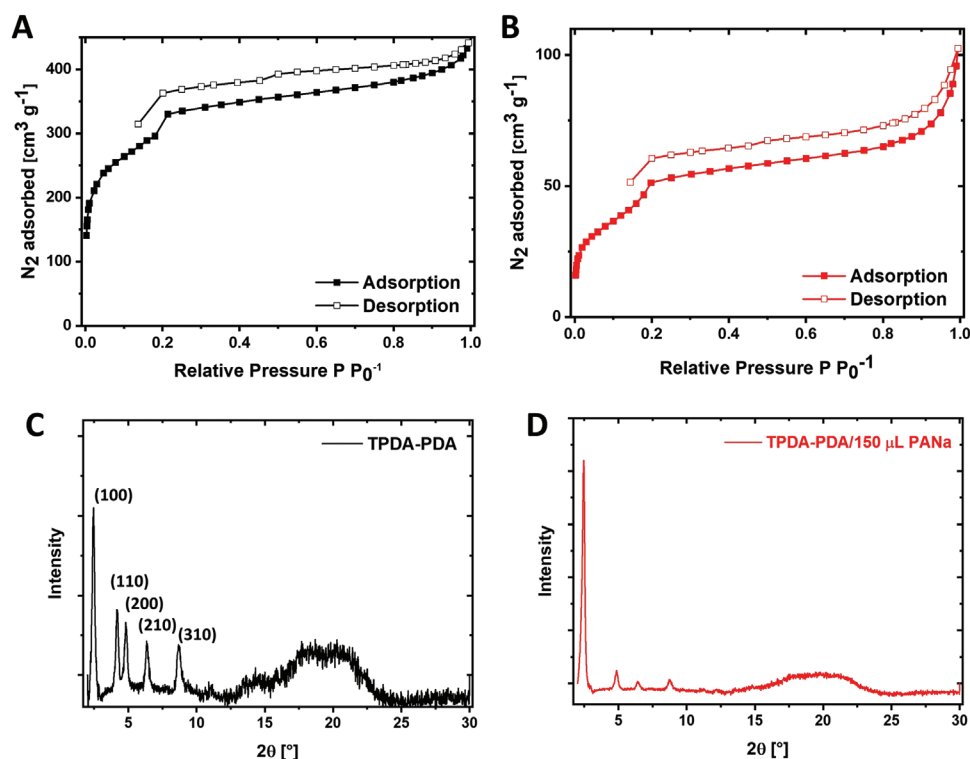


Figure 2. Nitrogen physisorption isotherms of A) TPDA-PDA and B) TPDA-PDA/150 μL PANa. Powder-X ray diffraction (PXRD) of C) pristine TPDA-PDA and D) TPDA-PDA/150 μL PANa.

and the COF/PANa blend, respectively, suggesting that the presence of PANa might induce a better thermal stability.^[19] Nitrogen (N_2) physisorption isotherms were acquired to determine the internal surface area of TPDA-PDA and TPDA-PDA/150 μL PANa. (Figure 2A,B) Both samples exhibit sorption isotherms featuring a mixture of type I and IV with two N_2 uptake steps, indicating the presence of micro- and mesopores.^[20] The calculated Brunauer, Emmett, Teller (BET) surface areas are 1100 and 173 $\text{m}^2 \text{g}^{-1}$ for TPDA-PDA and TPDA-PDA/150 μL PANa, respectively. The considerable surface area reduction proves the successful growth of PANa in the 1D COF channels, preventing N_2 uptake.^[19] Pore sizes were calculated from the N_2 isotherms using the density functional theory method with a cylindrical carbon pore model. (Figure S6, Supporting Information) Two pores were identified in the analyzed samples, with sizes of 2.14 and 3.22 nm for TPDA-PDA, and 2.14 and 3.10 nm for TPDA-PDA/150 μL PANa. PXRD spectrum of TPDA-PDA revealed high crystallinity of the COF (Figure 2C). The main peaks at 2.45° , 4.19° , 4.81° , 6.34° , and 8.68° are ascribed to the (100), (110), (200), (210), and (310) reflection planes, respectively, which were found being in good accordance with the simulation of a P6- symmetric structure model describing a Kagome structure.^[17] By definition, COFs are characterized by long-range order derived from the stacking of the planar sheets to form layered structures.^[21] In the XRD spectra, strong diffraction peaks at low angles are derived from the long-range order of uniform porous channels. However, when guests molecules/ions are adsorbed in the COF channels, but are non-uniformly dispersed, this may induce the damage of the long-range order of the framework, thus resulting in the disappearance of diffraction peaks at low values of 2θ .^[22]

Noteworthy, the crystallinity of TPDA-PDA is maintained when the sample with 150 μL of PANa is prepared, even though the disappearance of the diffraction from the (110) plane is observed, as a consequence of disrupted long-range framework order upon PANa polymerization (Figure 2D).

First, EIS was used to determine the influence of the concentration of PANa on the σ and the activation energy (E_a) for the conduction. The investigation was conducted in the frequency range of Hz–kHz, where ionic polarization can be determined.^[23] EIS measurements on pristine TPDA-PDA and TPDA-PDA/PANa blends were carried out in two different conditions: i) equilibration followed by measurements at the same temperature and humidity conditions, or ii) equilibration/activation followed by measurements under ambient conditions. The former allows to assess the conduction mechanism and the activation energy, by varying the equilibration and measurement temperature, keeping the RH fixed at 95%. The second case provides insight into the effect of the preliminary equilibration at high temperature and humidity which allows the activation of the SPEs. Indeed, a common and simple activation strategy in real-life use of FCs is to steam or boil the MEA prior to use. This practice allows the proper hydration of the SPE ensuring high σ , representing a solution to the concerning water management problem in PEMFCs.^[5,24]

Figures S7 and S8 (Supporting Information) show the Nyquist plots for TPDA-PDA and TPDA-PDA/PANa blends, containing 50, 100, 150, 200, and 250 μL of PANa over 40 mg of COF. The spectra were obtained at ambient conditions after equilibration at 65°C and vacuum or at 80°C and 95% RH, respectively. The values of pellet resistance and σ calculated

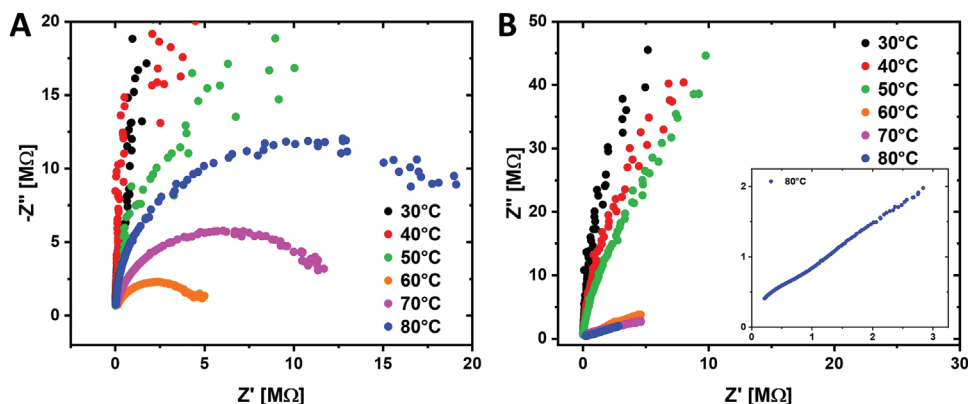


Figure 3. Nyquist plots obtained at 95% RH and variable temperature in the range of 30–80 °C for A) pristine TPDA-PDA and B) TPDA-PDA/150 μL PANa. The inset shows the response of TPDA-PDA/150 μL PANa at 80 °C.

from the fitting of the curves in Figure S8 (Supporting Information) are reported in Table S1 (Supporting Information). The fitting of the Nyquist plots was performed with the most appropriate equivalent circuit among the ones displayed in Figure S9 (Supporting Information) and σ was calculated from the equation in Figure S9 (Supporting Information). Table S1 (Supporting Information) shows that after activation at 80 °C and 95% RH, σ reaches a maximum of $2 \times 10^{-9} \pm 1 \times 10^{-9} \text{ S cm}^{-1}$ upon adding 150 μL of PANa to the COF TPDA-PDA, while the pristine COF's σ amounts to $1 \times 10^{-11} \pm 6 \times 10^{-12} \text{ S cm}^{-1}$. Furthermore, σ decreases upon increasing the concentration of the superadsorbent polymer in the COF/PANa blends. For this reason, the results obtained with TPDA-PDA will be compared with the TPDA-PDA/150 μL PANa blend from now on.

Depending on the experimental conditions the behavior of the two samples was found being remarkably different. **Figure 3** depicts the temperature-dependent conductivity of TPDA-PDA and TPDA-PDA/150 μL PANa. By keeping the RH constant at 95%, EIS measurements are performed equilibrating the sample at different temperatures in the range of 30–80 °C. Figure 3 and Table S2 (Supporting Information) overall show that the conductivity increases with the temperature. It is well known that temperature plays a crucial role in promoting σ , since it provides energy to overcome activation barriers for proton motion.^[11,25] Because of this reason, in the case of TPDA-PDA the conductivity values were extremely low ($\approx 10^{-11} \text{ S cm}^{-1}$) up to 50 °C, while they reached their maximum value ($1.4 \times 10^{-9} \text{ S cm}^{-1}$) at 60 °C, as evidenced by the appearance of a smaller semicircle in the Nyquist plot, which is due to a smaller charge transfer resistance of the pellet. When the temperature is increased to 70 and 80 °C, the conductivity decreases sequentially, most likely due to the removal of the adsorbed water molecules from the membrane.^[1] On the other hand, TPDA-PDA/150 μL PANa also exhibits low conductivity at temperatures <60 °C, yet the response is completely different in the range of 60–80 °C (Figure 3B). Indeed, the sample exhibits conductivity originating from two different charge transfer processes, as evidenced by the appearance of two semicircles in the Nyquist plot (see inset in Figure 3B). This behavior can be ascribed to the presence of two time scales for proton transport due to the coexistence of

long-range proton hopping and areas of the network having a low degree of percolation, most likely due to the inhomogeneous distribution of PANa within TPDA-PDA/150 μL PANa matrix.^[26] Furthermore, a linear tail at low frequencies is also visible in the spectrum, and can be associated with the formation of an electrical double layer between protons and electrons at the interface with the electrodes.^[27] The highest value of σ ($1.1 \times 10^{-8} \text{ S cm}^{-1}$) is found at 80 °C for TPDA-PDA/150 μL PANa, being one order of magnitude larger than the one obtained at 60 °C for TPDA-PDA. The temperature-dependent EIS study makes it possible to calculate the proton conduction E_a from the Arrhenius law: $\ln \sigma = \ln \sigma_0 + \frac{-E_a}{k_B T}$, where k_B is the Boltzmann constant ($1.38 \times 10^{-23} \text{ J K}^{-1}$) and T is the absolute temperature in K. Figure S10A (Supporting Information) reflects the behavior already evidenced by the Nyquist plot for TPDA-PDA, with the conductivity abruptly starting to increase at 50 °C, reaching its maximum at 60 °C and then decreasing. Taking into account that the highest operating temperature for TPDA-PDA is 60 °C, the fitting of the corresponding Arrhenius plot has been performed in the range of 30–60 °C (Figure S10A, Supporting Information). The E_a for proton conduction corresponds to 1.08 eV, which clearly means that the poor σ of the pristine COF occurs by the vehicle mechanism.^[28] It has been reported that values of $E_a > 0.4 \text{ eV}$ indicate a vehicle mechanism of conduction: within such a scenario, the proton conducting species (water in our case) migrate within the network, carrying the protons (H_3O^+).^[29] In Figure S10B (Supporting Information), two regimes can be recognized for TPDA-PDA/150 μL PANa: both at low (30–50 °C) and high temperature (60–80 °C) σ increases linearly with T and from the linear fitting of the data it is found that within the first range the E_a amounts to 0.45 eV, which means that the conduction occurs through a mixed Grotthus-vehicle mechanism.^[30] This implies the hopping of protons through a hydrogen-bonded network, whose formation may be aided by the presence of the superadsorbent polymer.^[31] On the other hand, at high temperatures (60–80 °C) E_a reaches a value of 0.63 eV, which is coherent with a vehicle mechanism, meaning that there is enough energy also for the movement of proton carriers through the network.^[10]

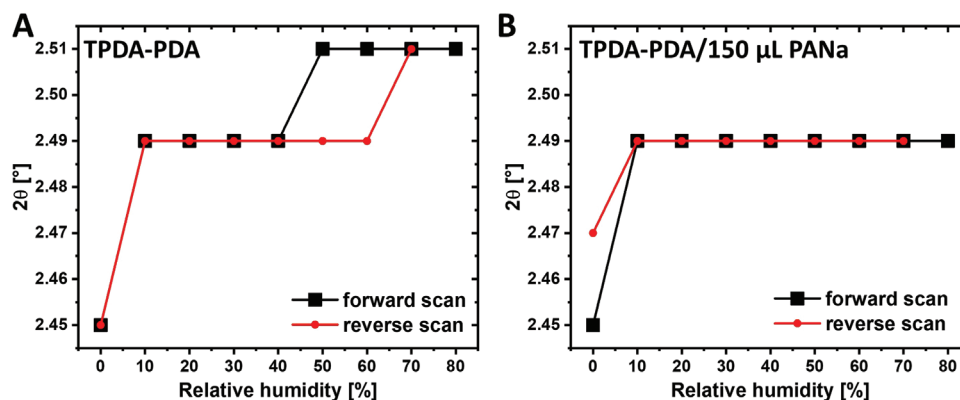


Figure 4. (100) plane diffraction as a function of relative humidity (RH) for A) pristine TPDA-PDA and B) TPDA-PDA/150 μL PANa. Black lines represent the variation of 2θ with increased RH, while red lines stand for its variation with decreased RH. The first and last points are acquired after drying the sample at 65 $^{\circ}\text{C}$ in vacuum for 1 h.

Being the high crystallinity one of the greatest advantages in employing COFs as proton conductors,^[12] we propose for the first time, to the best of our knowledge, an elucidation of the structure at variable RH by XRD, in order to gain greater insight into the proton conduction mechanism. **Figure 4** shows that the diffraction from the (100) plane appears at 2.45 $^{\circ}$ for both the pristine TPDA-PDA and TPDA-PDA/150 μL PANa. In the former case, this peak shifts from 2.45 $^{\circ}$, corresponding to a lattice distance of 3.61 nm, to 2.49 $^{\circ}$ (3.55 nm) upon increasing the RH to 10% and such a value remains stable in the interval 10–40% RH. The peak position shifts to 2.51 $^{\circ}$ (3.52 nm) when RH increases to 50–80%. At this point, the sample is equilibrated at reduced RH for the reverse scan. The peak does not undergo any shift until 60% RH, when swelling occurs, obtaining a lattice distance of 3.55 nm along the direction of the (100) plane. Finally, when the sample is dried again at 65 $^{\circ}\text{C}$ and vacuum, the initial peak position at 2.45 $^{\circ}$ is restored (Figure 4A). As far as TPDA-PDA/150 μL PANa is concerned, Figure 4B shows that the same peak shifts from 2.45 $^{\circ}$ to 2.49 $^{\circ}$ (3.55 nm) when RH is increased to 10% and this value is maintained until 80% RH. In the reverse RH scan, we do not observe any variation in the peak position until the sample is dried: at this point, the diffraction from the (100) plane appears at 2.47 $^{\circ}$ (3.58 nm). These evidences indicate that the presence of PANa in the sample does not allow the lattice distance to decrease <3.55 nm; furthermore, probably as a consequence of its superadsorbing nature, by drying the sample the initial distance is not restored completely. Overall, the results suggest that the proton conduction in the studied materials could take place because of the decrease in the (100) plane lattice distance, which may be due to the strengthening of the stacking interaction^[32] through the H-bonding, promoting the proton hopping. In addition, the exposure of both TPDA-PDA and TPDA-PDA/150 μL PANa to humidity results in the appearance of a new peak at 3.3 $^{\circ}$, a general variation of the peaks relative intensities and an increase of the full-width at half maximum (FWHM) of the peaks.^[33] In particular, we measured that it increases from 0.3 to 0.6 $^{\circ}$ in the case of the diffraction from the (210) plane (Figure S11, Supporting Information).

The reported results indicate that the proposed SPE (TPDA-PDA/150 μL PANa) could find application in LT-FCs, operating

at 80 $^{\circ}\text{C}$. Considering that the major limitation of LT-FCs is the necessity to be operated at high RH, leading to serious water management problems, we investigated an equilibration/activation procedure to facilitate the preservation of high σ at low RH. By analyzing the second set of EIS measurements, we can conclude that pristine TPDA-PDA does not exhibit any significant conductivity when measuring at ambient conditions neither when this is preceded by equilibration/activation at high temperature and vacuum nor at high RH. Indeed, **Figure 5** shows the Bode plots of the impedance phase angle in both situations. A phase angle at -90° over the whole frequency range suggests that the material behaves similarly to a capacitor.^[34] One can imagine that the concentration of proton carriers is so low that the only phenomenon taking place is the accumulation of electrons at the electrodes.^[27] On the other hand, equilibration of TPDA-PDA/150 μL PANa at high temperature and vacuum or high RH induces two distinct responses. In the former case, Figure 5A shows that the addition of PANa does not influence the conductivity in dry state, since no water can be adsorbed to vehicle the conduction. However, by activating the sample at 80 $^{\circ}\text{C}$ and 95% RH, probably thanks to the superadsorbing ability of the polymer, a resistive behavior is visible at medium and low frequencies (Figure 5B). These findings can be rationalized by considering that at high frequency the only species which could move among the electrodes are the electrons, while, when the intercurrent time among the alternating current (AC) polarity shift increases, also the protons are able to migrate toward the electrodes, creating eventually an electrical double layer at the interface. These findings open perspectives for the application of these materials as SPEs in LT-PEMFCs, which operate at least at ≈ 60 –80 $^{\circ}\text{C}$, since sufficient driving force should be provided for the catalysis of the anodic and cathodic reactions. However, humidification during operation is not ideal, since it limits the real-life applications, reducing the portability and cost-effectiveness of the devices. The proposed method of equilibration/activation at high temperature and RH prior to ambient conditions operation could represent a valid solution to the concerning water management problem in PEMFCs.

The study of dielectric relaxation behavior in ion-conducting polymer composite materials has become an interesting

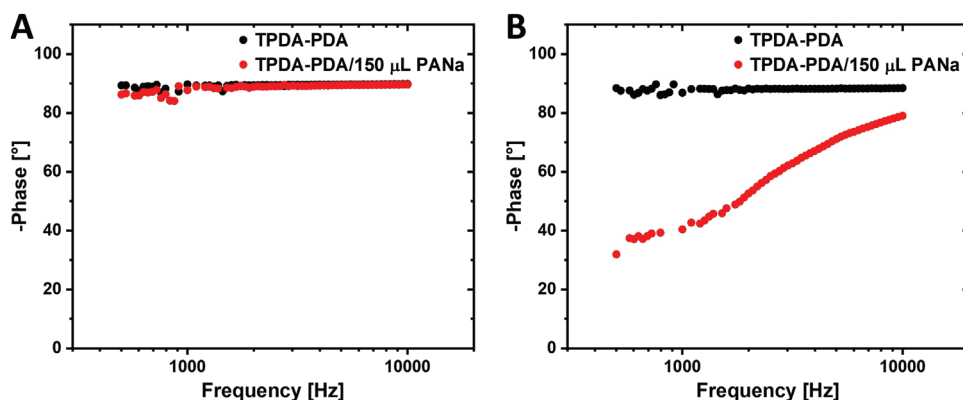


Figure 5. Bode plots of the impedance phase angle for TPDA-PDA and TPDA-PDA/150 μL PANa obtained at ambient conditions after equilibration at A) 65 $^{\circ}\text{C}$ and vacuum, and B) 80 $^{\circ}\text{C}$ and 95% RH.

research area for understanding the ionic transport properties of these novel materials.^[35,36] To the best of our knowledge, dielectric studies on COFs as proton-conducting materials have not been performed yet. Here, EIS was employed also to shed a light onto the dielectric properties of the studied COF as a SPE. Indeed, by applying AC potential at a variable frequency, we can determine both the complex electrochemical impedance (Z^*), modulus (M^*), and permittivity (ϵ^*). Conduction can take place in the bulk material and at the interface with the electrodes through a series of charge transfer processes. By plotting the variation of these entities with frequency, the relaxation frequencies can be determined. Although the plots of Z^* , M^* , and

ϵ^* versus frequency represent the same relaxation phenomena, each representation allows extracting different and complementary information about the analyzed system.^[23] The frequency response of the real (Z') and imaginary part ($-Z''$) of the impedance is shown in **Figure 6A,B** for TPDA-PDA and TPDA-PDA/150 μL PANa, while **Figure S12A** (Supporting Information) exhibits the frequency response of the same entities for TPDA-PDA/100 μL PANa. Z' accounts for Ohmic resistance of the pellet, while $-Z''$ is related to the non-Ohmic resistance, being a consequence of the short-range mobility. $-Z''$ generally exhibits a maximum $\omega_{\text{max}}^{Z''}$, which is due to the collective relaxation of dipoles when the sample is exposed to an oscillating electric

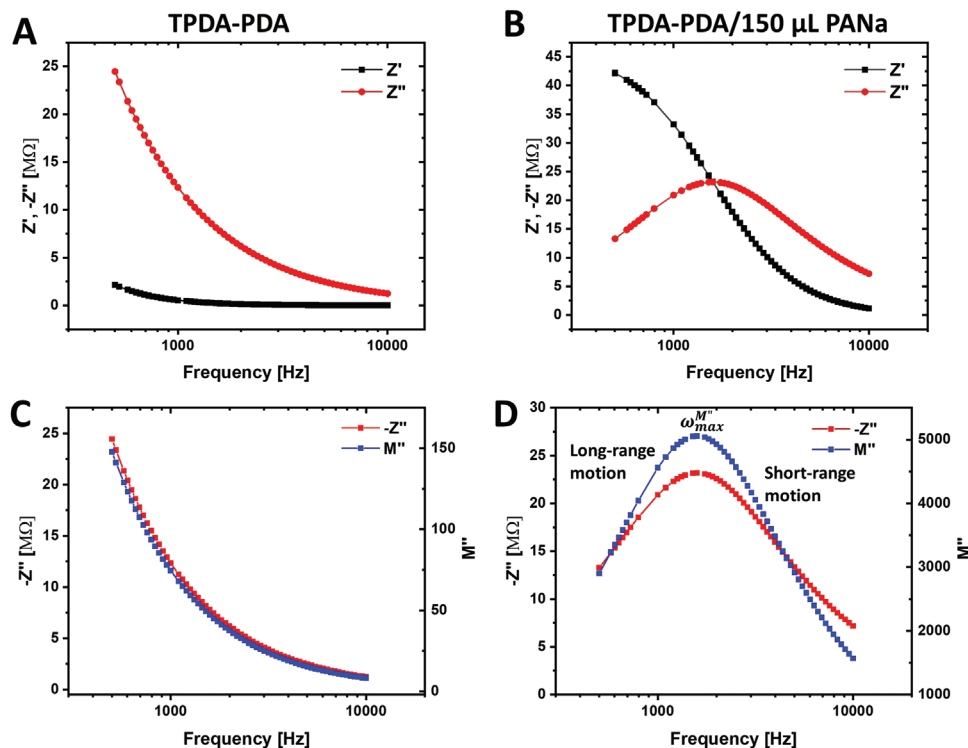


Figure 6. Frequency dependence of the A,B) real (Z') and imaginary ($-Z''$) part of the impedance and C,D) imaginary ($-Z''$) part of the impedance and imaginary part of the electric modulus (M'') for (A,C) TPDA-PDA and (B,D) TPDA-PDA/150 μL PANa. Data were extracted from the impedance measurements conducted at ambient conditions after equilibration/activation at 80 $^{\circ}\text{C}$ and 95% RH.

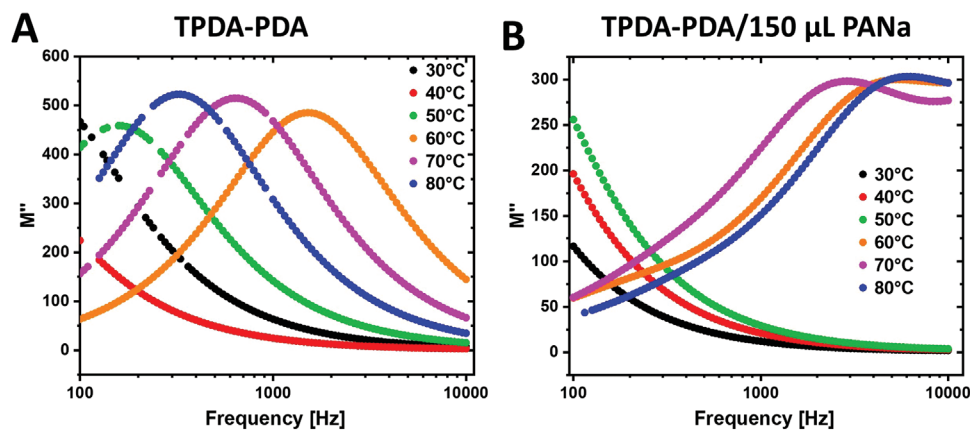


Figure 7. Frequency dependence of the imaginary part of the modulus (M'') as a function of the temperature for A) TPDA-PDA and B) TPDA-PDA/150 μL PANa. Data were extracted from the impedance measurements conducted at 95% RH and varying temperatures.

field. In an ideal Debye relaxation regime, $-Z''$ approaches zero for frequencies smaller than $\omega_{\max}^{Z''}$ and it decreases monotonically for $\omega > \omega_{\max}^{Z''}$. Deviations from this behavior can be ascribed to conduction inhomogeneity, due to the presence of non-conducting domains in the sample, accumulated charges at the interface, etc. In the case of pristine TPDA-PDA, the Z'' relaxation peak is not visible in the studied frequency range (Figure 6A), while it exhibits a maximum in the case of TPDA-PDA/100 μL PANa and TPDA-PDA/150 μL PANa at 1380 and 1585 Hz, respectively (Figure 6B; Figure S12A, Supporting Information). From $\omega_{\max}^{Z''}$ it is possible to calculate the relaxation time constant as $\tau = 1/2\pi\omega_{\max}^{Z''}$. It was found that τ decreases from 1.2×10^{-4} to 1.0×10^{-4} s when PANa content is increased from 100 to 150 μL , meaning that the increased PANa concentration ensures a more efficient charge carrier transport.^[35,37] In the case of pristine TPDA-PDA, the relaxation time is clearly longer, since $\omega_{\max}^{Z''}$ falls < 500 Hz. The Z' , $-Z''$ versus frequency plots allow also to identify the frequency at which Z' and Z'' curves cross (ω_{cross}). A system is in a Debye relaxation regime when $\omega_{\max}^{Z''} \approx \omega_{\text{cross}}$. Once again, we cannot do any consideration for pristine TPDA-PDA, while the coincidence of $\omega_{\max}^{Z''}$ and ω_{cross} for both the samples with 100 μL and 150 μL of PANa suggests that these systems are close to a Debye relaxation regime.

The electric modulus M^* is closely related to the impedance measured by EIS. In particular, its real part (M') is calculated as

$$M' = C_0 \omega Z'' = \epsilon_0 \omega Z'' \frac{A}{l} \quad (1)$$

Where ϵ_0 is the permittivity of vacuum (8.854×10^{-12} Fm $^{-1}$), ω is the frequency, Z'' is the imaginary part of the impedance and A and l are the area and the thickness of the pellet, respectively. The imaginary part of the modulus M'' is proportional to Z' through the same relationship. These proportionalities imply that M' accounts for localized short-range motion of charges, while M'' is related to the (non-local) long-range motions. Figure S12B (Supporting Information) and Figure 6D show that M'' exhibits a maximum $\omega_{\max}^{M''}$ at 1380 and 1585 Hz in the case of TPDA-PDA/100 μL PANa and TPDA-PDA/150 μL PANa, respectively. Both systems follow the equality $\omega_{\max}^{Z''} = \omega_{\text{cross}} = \omega_{\max}^{M''}$ which reflects the absence of dispersion of relaxation times. Furthermore, M'' maximum value reflects the transition from

long-range ($\omega < \omega_{\max}^{M''}$) to short-range motion, when the charge carriers are not able to follow the fast changes of the oscillating electrical field.^[23,38,39] The higher value of $\omega_{\max}^{M''}$ for the sample with 150 μL of PANa suggests that the frequency range for non-local motion is wider.

Figure 7 illustrates the temperature dependence of $\omega_{\max}^{M''}$ for TPDA-PDA and TPDA-PDA/150 μL PANa when EIS measurements are performed at 95% RH and varying temperatures. Overall, the modulus plot maintains its shape with increasing temperature, implying that the distribution of relaxation times is not dependent on the temperature. The highest $\omega_{\max}^{M''}$ value for TPDA-PDA amounts to 1513 Hz at 60 $^{\circ}\text{C}$, with a τ of 1×10^{-4} s, while they are found to correspond to 6606 Hz and 2×10^{-5} s for TPDA-PDA/150 μL PANa at 80 $^{\circ}\text{C}$. These findings evidence once again that the addition of 150 μL of PANa induces an extension of the frequency range for the long-range motion of charge carriers. The frequency and τ values at every analyzed temperature are reported in Tables S3 and S4 (Supporting Information). An increase in relaxation frequency with a decrease in relaxation time suggests an increase in the charge carriers' mobility. The thermal energy provided with the increasing temperature facilitates the charge carriers to move toward the electrodes before the polarity switch of the AC.^[39]

3. Conclusion

In this work, we present a simple strategy to improve the performance of poor proton conductors based on COFs, upon addition of a superadsorbent polymer. EIS studies at high RH and variable temperature reveal that the blending of TPDA-PDA with 150 μL PANa ensures one order of magnitude enhanced σ compared to the pristine TPDA-PDA, with the additional bonus of being able to operate at higher temperature (80 vs 60 $^{\circ}\text{C}$). The E_a of 0.45 and 0.63 eV at low and high temperature suggest a mixed Grotthuss-vehicle mechanism, coherent with the coexistence of proton hopping through a hydrogen-bonded network, aided by the presence of the superadsorbent polymer, and the movement of proton carriers through the network. Interestingly, we noticed that the TPDA-PDA/150 μL PANa can preserve good σ at low RH, after equilibration/activation

at high temperature and RH. EIS data are well supported by an in-depth study of the humidity-dependent X-ray diffraction, showing the reduction of the (100) plane lattice distance upon increasing RH, which could be related to the strengthening of the stacking interaction through the H-bonding, thereby promoting the proton hopping. Furthermore, an extensive study of the dielectric properties of COFs as proton-conducting materials has been proposed for the first time in literature, to the best of your knowledge. We determined a Debye relaxation regime for TPDA-PDA/PANa blends, with ω_{\max}^M increasing from 1380 to 1585 Hz when the PANa content increased from 100 to 150 μL in the blend. Besides, the temperature-dependent dielectric study revealed that the width of frequency range for a long-range motion of charge carriers in the electrolyte increased when comparing the pristine COF and the TPDA-PDA/150 μL PANa at their maximum operating temperatures, with ω_{\max}^M increasing from 1513 to 6606 Hz. Overall, we were able to unveil the effect of a superadsorbent polymer on a poorly proton-conducting COF correlating the variation of the material's spectroscopic fingerprint (IR and XRD) with its proton conduction performance (EIS) and dielectric properties, also presenting an efficient SPE activation strategy to preserve σ at ambient conditions, which represents a viable solution to the concerning water management problem in PEMFCs.

4. Experimental Section

Materials: *N,N,N',N'*-tetrakis(4-aminophenyl)-1,4-phenylenediamine (98%) was purchased from abcr GmbH Germany, terephthalaldehyde (99%) was purchased from Merck, mesitylene (98%), benzyl alcohol (99%), and acetic acid (glacial) were purchased from Fisher Scientific. Acrylic acid (99%), *N,N'*-Methylenebis(acrylamide) (99%), ammonium persulfate (98%) were acquired from Merck. Sodium hydroxide (NaOH pellets) was purchased from VWR. Milli-Q grade water was used in all described experiments.

Methods: *COF TPDA-PDA synthesis.* COF TPDA-PDA synthesis has been conducted as a modification of Hao's method,^[17] Scheme 1A. In a 35 mL pressure-resistant Schlenk tube, 101 mg of terephthalaldehyde (PDA, 0.75 mmol) and 238 mg of *N,N,N',N'*-tetrakis(4-aminophenyl)-1,4-phenylenediamine (TPDA, 0.5 mmol) were suspended in a mixture of benzyl alcohol (4 mL), mesitylene (4 mL), acetic acid (1 mL), and H_2O (0.2 mL). After sealing the tube, the suspension was degassed by three freeze-pump-thaw cycles and sonicated for 30 min. The condensation reaction yielding TPDA-PDA COF was carried at 120 °C for 72 h in an oven. After cooling down, the solid precipitate was filtered off and washed thoroughly with *N,N*-dimethylformamide. The wet powders were then subjected to Soxhlet extraction with tetrahydrofuran for 24 h. Next, solvent exchange was performed by 24 h immersion of the powders in 50 mL of *n*-pentane. Finally, the solid was filtered and dried under vacuum at 80 °C overnight. The TPDA-PDA COF was obtained as red insoluble powder, with a yield of 72%.

TPDA-PDA/PANa blends preparation. A schematic representation of the COF TPDA-PDA/PANa blend preparation is shown in Scheme 1B. TPDA-PDA/PANa blends were obtained as a modification of Yang's method.^[19] First, sodium polyacrylate (PANa) was synthesized in an ice bath by adding 5 mL of an aqueous 10 M NaOH solution to a dispersion of acrylic acid (3.6 mL) in 5 mL of water. Subsequently, *N,N'*-methylenebis(acrylamide) and ammonium persulfate were added to the solution yielding a final concentration of 0.7 and 18 mM, respectively. The as-prepared solution was left under stirring for 30 min, before adding different contents of it (50, 100, 150, 200, 250 μL) to aliquots of 40 mg of TPDA-PDA. Thermal polymerization of PANa occurred when the TPDA-PDA/PANa blends were incubated at 65 °C for 2 h, after which they were thoroughly washed with water and

filtered. The powders were dried on the filter paper for 2 h at 65 °C and then transferred in vials. Complete drying was performed at 65 °C and vacuum overnight.

Characterization: Scanning electron microscopy (SEM) images were recorded by using a FEI Quanta 250 FEG Scanning Electron Microscope, operating in a high vacuum mode, after coating the substrate with gold using a sputter coater (ambient temperature, pressure in 10^{-4} mbar range in a N_2 atmosphere, sputtered for 20 s from a solid gold target at a current of 60 mA). Powder X-ray diffraction (PXRD) spectra were recorded using a D8 Advanced Bruker diffractometer (2θ resolution: $\pm 0.01^\circ$) in the Bragg–Brentano geometry. The diffractometer was equipped with a front monochromator (Cu $K\alpha 1$ wavelength $\lambda = 0.154\ 056\ \text{nm}$) and a LynxEye_2 detector (ID mode). The X-ray beam was nickel-filtered to reduce the intensity of the Cu $K\beta$ X-rays. XRD data were collected from 2 to 30° (2θ) with a step size of 0.01° at a scanning rate of 0.1 s per step. The sample was placed inside a Cryo & Humidity Chamber CHC plus+ Anton Paar mounted on the Bruker diffractometer. The atmosphere in the CHC plus+ Chamber is controlled by a CCU 100 combined Control Unit and a MHG-32 Modular Humidity Generator. Analyses were performed at 25 °C in the air with controlled relative humidity varying between 10% and 80%. Fourier transform–infrared (FT–IR) spectra were acquired with a ThermoScientific Nicolet iS50 FT–IR Spectrometer equipped with ATR Diamond and a DTGS KBr detector. Thermogravimetric analysis (TGA) decomposition curves were recorded in the range of 25–1000 °C operating under a nitrogen atmosphere, with a thermal step of 10 °C min^{-1} on a Mettler Toledo TGA/SDTA851e system. Nitrogen sorption isotherms were recorded without a solvent exchange using a Micromeritics ASAP 2020 instrument at 77K within pressure ranges of $P/P_0 = 0.001$ –1. The samples were activated at 373 K for 480 min before analysis. Brunauer, Emmett, Teller (BET) surface area has been evaluated up to 0.3 relative pressure. Pore sizes were calculated from the nitrogen isotherms using the density functional theory (DFT) model for cylindrical pores. Electrochemical impedance spectroscopy (EIS) measurements were conducted on pelletized samples: 40 mg of TPDA-PDA or TPDA-PDA/PANa blends were pressed under 10 tons with a Specac press machine. The as-obtained pellets were sandwiched between two gold electrodes. The latter were prepared sputtering 100 nm of gold on glass slides using a sputter coater (ambient temperature, pressure in 10^{-4} mbar range in a nitrogen atmosphere, sputtered for 240 s from a solid gold target at a current of 60 mA). EIS was performed in a two-electrode configuration (counter- and reference electrode vs working electrode) with an Autolab PGSTAT204 Potentiostat/Galvanostat instrument with a FRA32M module, applying a 0.2 V DC bias (5 s waiting time), scanning in the 100 Hz–10 kHz range with a 0.1 V amplitude. Sample equilibration at 65 °C and vacuum was performed in a ThermoScientific Vacutherm vacuum oven, while the equilibration at 95% RH and varying temperature in the range of 30–80 °C was carried out using a Benchtop Temperature and Humidity Test Chamber TH-80A from Xi'an LIB Environmental Simulation Industry. The equilibration time for the temperature-dependent EIS measurements was set at 1 h, while the samples were equilibrated at 80 °C and 95% RH for 6 h for the activation.

Supporting Information

Supporting Information is available from the Wiley Online Library or from the author.

Acknowledgements

The authors acknowledge the financial support from the European Commission through the Marie Skłodowska-Curie project ULTIMATE (GA-813036), the Interdisciplinary Thematic Institute SysChem via the IdEx Unistra (ANR-10-IDEX-0002) within the program Investissement d'Avenir program, the International Center for Frontier Research in Chemistry (icFRC), the Institut Universitaire de France (IUF). The authors thank Professors Jean–Marc Planeix and Mir Wais Hosseini for their support in the BET analysis.

Conflict of Interest

The authors declare no conflict of interest.

Author Contributions

S.G. performed conceptualization, methodology, writing—original draft, review and editing, data curation, formal analysis, EIS, IR, SEM, TGA investigations. L.C. performed COF synthesis and XRD investigation. F.R. performed XRD investigation. N.I. performed BET analysis. A.C. performed writing—review and editing and supervision. P.S. performed writing—review and editing, supervision and funding acquisition.

Data Availability Statement

The data that support the findings of this study are available from the corresponding author upon reasonable request.

Keywords

covalent organic frameworks, hybrid materials, proton conductivity, solid polymer electrolytes

Received: February 11, 2023

Revised: March 21, 2023

Published online:

- [1] R. Sahoo, S. Mondal, S. C. Pal, D. Mukherjee, M. C. Das, *Adv. Energy Mater.* **2021**, *11*, 2102300.
- [2] W. R. W. Daud, R. E. Rosli, E. H. Majlan, S. A. A. Hamid, R. Mohamed, T. Husaini, *Renewable Energy* **2017**, *113*, 620.
- [3] P. Ramaswamy, N. E. Wong, G. K. H. Shimizu, *Chem. Soc. Rev.* **2014**, *43*, 5913.
- [4] a) R. Haider, Y. Wen, Z.-F. Ma, D. P. Wilkinson, L. Zhang, X. Yuan, S. Song, J. Zhang, *Chem. Soc. Rev.* **2021**, *50*, 1138; b) T. Lochner, R. M. Kluge, J. Fichtner, H. A. El-Sayed, B. Garlyyev, A. S. Bandarenka, *ChemElectroChem* **2020**, *7*, 3545.
- [5] K. Jiao, M. Ni, *Int. J. Energy Res.* **2017**, *41*, 1793.
- [6] a) P. Pei, X. Fu, Z. Zhu, P. Ren, D. Chen, *Int. J. Hydrogen Energy* **2022**, *47*, 24897; b) X.-Z. Yuan, S. Zhang, J. C. Sun, H. Wang, *J. Power Sources* **2011**, *196*, 9097.
- [7] a) S. Kandambeth, K. Dey, R. Banerjee, *J. Am. Chem. Soc.* **2019**, *141*, 1807; b) H. S. Sasmal, A. Kumar Mahato, P. Majumder, R. Banerjee, *J. Am. Chem. Soc.* **2022**, *144*, 11482; c) L. Cusin, H. Peng, A. Ciesielski, P. Samorì, *Angew. Chem., Int. Ed.* **2021**, *60*, 14236; d) J. L. Segura, M. J. Mancheño, F. Zamora, *Chem. Soc. Rev.* **2016**, *45*, 5635; e) L. Xu, S.-Y. Ding, J. Liu, J. Sun, W. Wang, Q.-Y. Zheng, *ChemComm* **2016**, *52*, 4706.
- [8] a) K. Geng, T. He, R. Liu, S. Dalapati, K. T. Tan, Z. Li, S. Tao, Y. Gong, Q. Jiang, D. Jiang, *Chem. Rev.* **2020**, *120*, 8814; b) C. S. Diercks, O. M. Yaghi, *Science* **2017**, *355*, eaal1585.
- [9] a) Y. Lu, Z.-B. Zhou, Q.-Y. Qi, J. Yao, X. Zhao, *ACS Appl. Mater. Interfaces* **2022**, *14*, 37019; b) M.-H. Li, Z. Yang, Z. Li, J.-R. Wu, B. Yang, Y.-W. Yang, *Chem. Mater.* **2022**, *34*, 5726; c) G. Das, B. P. Biswal, S. Kandambeth, V. Venkatesh, G. Kaur, M. Addicoat, T. Heine, S. Verma, R. Banerjee, *Chem. Sci.* **2015**, *6*, 3931; d) H. Wang, H. Wang, Z. Wang, L. Tang, G. Zeng, P. Xu, M. Chen, T. Xiong, C. Zhou, X. Li, D. Huang, Y. Zhu, Z. Wang, J. Tang, *Chem. Soc. Rev.* **2020**, *49*, 4135; e) D. Pakulski, V. Montes-García, A. Gorczyński, W. Czepa, T. Chudziak, P. Samorì, A. Ciesielski, *J. Mater. Chem. A* **2022**, *10*, 16685.
- [10] P. Jhariat, P. Kumari, T. Panda, *CrystEngComm* **2020**, *22*, 6425.
- [11] S. Chandra, T. Kundu, S. Kandambeth, R. BabaRao, Y. Marathe, S. M. Kunjir, R. Banerjee, *J. Am. Chem. Soc.* **2014**, *136*, 6570.
- [12] Z.-C. Guo, Z.-Q. Shi, X.-Y. Wang, Z.-F. Li, G. Li, *Coord. Chem. Rev.* **2020**, *422*, 213465.
- [13] S. Chandra, T. Kundu, K. Dey, M. Addicoat, T. Heine, R. Banerjee, *Chem. Mater.* **2016**, *28*, 1489.
- [14] Z. Guo, M. Perez-Page, J. Chen, Z. Ji, S. M. Holmes, *J. Energy Chem* **2021**, *63*, 393.
- [15] B. Shi, X. Pang, S. Li, H. Wu, J. Shen, X. Wang, C. Fan, L. Cao, T. Zhu, M. Qiu, Z. Yin, Y. Kong, Y. Liu, M. Zhang, Y. Liu, F. Pan, Z. Jiang, *Nat. Commun.* **2022**, *13*, 6666.
- [16] K. Biradha, A. Goswami, R. Moi, S. Saha, *Dalton Trans.* **2021**, *50*, 10655.
- [17] Q. Hao, Z.-J. Li, B. Bai, X. Zhang, Y.-W. Zhong, L.-J. Wan, D. Wang, *Angew. Chem., Int. Ed.* **2021**, *60*, 12498.
- [18] M. Rogojerov, B. Jordanov, G. Keresztury, *J. Mol. Struct.* **2000**, *550–551*, 455.
- [19] J. Yang, C. Xie, Q. Yang, S. Wang, Y. Gao, J. Ji, Z. Du, Z. Kang, R. Wang, D. Sun, *ChemComm* **2022**, *58*, 1131.
- [20] J. M. Rotter, R. Guntermann, M. Auth, A. Mähringer, A. Sperlich, V. Dyakonov, D. D. Medina, T. Bein, *Chem. Sci.* **2020**, *11*, 12843.
- [21] X. Feng, X. Ding, D. Jiang, *Chem. Soc. Rev.* **2012**, *41*, 6010.
- [22] J. Cai, X. Wang, Y. Zhou, L. Jiang, C. Wang, *Phys. Chem. Chem. Phys.* **2016**, *18*, 10864.
- [23] V. F. Lvovich, in *Impedance Spectroscopy: Applications to Electrochemical and Dielectric Phenomena*, Wiley, Hoboken **2012**.
- [24] T. A. M. Suter, K. Smith, J. Hack, L. Rasha, Z. Rana, G. M. A. Angel, P. R. Shearing, T. S. Miller, D. J. L. Brett, *Adv. Energy Mater.* **2021**, *11*, 2101025.
- [25] P. C. Rieke, N. E. Vanderborgh, *J. Membr. Sci.* **1987**, *32*, 313.
- [26] D. C. Sabarirajan, J. Liu, Y. Qi, A. Perego, A. T. Haug, I. V. Zenyuk, *J. Electrochem. Soc.* **2020**, *167*, 084521.
- [27] T. Sung, S. D. Namgung, J. Lee, I. R. Choe, K. T. Nam, J.-Y. Kwon, *RSC Adv.* **2018**, *8*, 34047.
- [28] a) Z. Guo, Y. Zhang, J. Liu, B. Han, G. Li, *New J. Chem.* **2021**, *45*, 16971; b) Z. Sun, S. Yu, L. Zhao, J. Wang, Z. Li, G. Li, *Chemistry* **2018**, *24*, 10829.
- [29] a) J. Escorihuela, R. Narducci, V. Compañ, F. Costantino, *Adv. Mater. Interfaces* **2019**, *6*, 1801146; b) D.-W. Lim, M. Sadakiyo, H. Kitagawa, *Chem. Sci.* **2019**, *10*, 16.
- [30] X. Meng, H.-N. Wang, S.-Y. Song, H.-J. Zhang, *Chem. Soc. Rev.* **2017**, *46*, 464.
- [31] Z. Yang, P. Chen, W. Hao, Z. Xie, Y. Feng, G. Xing, L. Chen, *Chemistry* **2021**, *27*, 3817.
- [32] T. Sick, J. M. Rotter, S. Reuter, S. Kandambeth, N. N. Bach, M. Döblinger, J. Merz, T. Clark, T. B. Marder, T. Bein, D. D. Medina, *J. Am. Chem. Soc.* **2019**, *141*, 12570.
- [33] C. Kang, Z. Zhang, V. Wee, A. K. Usadi, D. C. Calabro, L. S. Baugh, S. Wang, Y. Wang, D. Zhao, *J. Am. Chem. Soc.* **2020**, *142*, 12995.
- [34] N. Turetta, M.-A. Stoeckel, R. Furlan de Oliveira, F. Devaux, A. Greco, C. Cendra, S. Gullace, M. Gicevičius, B. Chattopadhyay, J. Liu, G. Schweicher, H. Siringhaus, A. Salleo, M. Bonn, E. H. G. Backus, Y. H. Geerts, P. Samorì, *J. Am. Chem. Soc.* **2022**, *144*, 2546.
- [35] Z. Liu, K. Zhang, G. Huang, S. Bian, Y. Huang, X. Jiang, Y. Pan, Y. Wang, X. Xia, B. Xu, G. Zhang, *Chem. Eng. J.* **2022**, *433*, 133550.
- [36] A. Karmakar, A. Ghosh, *Curr. Appl. Phys.* **2012**, *12*, 539.
- [37] S. S. Batool, Z. Imran, K. Rasool, J. Ambreen, S. Hassan, S. Arif, M. Ahmad, M. A. Rafiq, *Sci. Rep.* **2020**, *10*, 2775.
- [38] S. F. Chérif, A. Chérif, W. Dridi, M. F. Zid, *Arabian J. Chem.* **2020**, *13*, 5627.
- [39] S. Manzoor, S. Husain, A. Somvanshi, M. Fatema, *J. Appl. Phys.* **2020**, *128*, 064101.